

Strong Coupling Between RF Photons and Plasmons of Electrons on Liquid Helium

Asher Jennings,^{1,*} Ivan Grytsenko,¹ Thomas Giovansili,^{1,2} Itay Josef Barabash,^{1,3} Oleksiy Rybalko,^{1,4} Yiran Tian,^{1,5} Jung Wang,¹ Hiroki Ikegami,^{1,6} and Erika Kawakami^{1,7,†}

¹*Center for Quantum Computing, RIKEN, Wako, Saitama 351-0198, Japan*

²*École Polytechnique, Route de Saclay, Palaiseau Cedex 91128, France*

³*School of Computer Science, McGill University, Montreal, Quebec H3A 2K6, Canada*

⁴*Physics of Quantum Fluids and Crystals, B. Verkin Institute for Low Temperature Physics and Engineering of the National Academy of Sciences of Ukraine, Kharkiv 61103, Ukraine*

⁵*Institute of Physics, Kazan Federal University, Kazan 420008, Republic of Tatarstan, Russian Federation*

⁶*Beijing National Laboratory for Condensed Matter Physics, Institute of Physics, Chinese Academy of Sciences, Beijing 100190, China*

⁷*Pioneering Research Institute, RIKEN, Wako, Saitama 351-0198, Japan*

(Dated: February 2, 2026)

Plasmons, arising from the collective motion of electrons, can interact strongly with electromagnetic fields or photons; this capability has been exploited across a broad range of applications, from chemical reactivity to biosensing. Recently, there has been growing interest in plasmons for applications in quantum information processing. Electrons floating on liquid helium provide an exceptionally clean, disorder-free system and have emerged as a promising platform for this purpose. In this work, we establish this system as a tunable plasmon–photon hybrid platform. We demonstrate strong coupling between floating-electron plasmons and radio-frequency (RF) photons confined in an LC resonator. Time-resolved measurements reveal coherent oscillatory energy exchange between the plasmonic and photonic modes, providing direct evidence of their coherent coupling. These results represent a step towards cavity quantum electrodynamics with a floating-electron plasmon coupled to a resonator. Furthermore, the LC resonator serves as a sensitive probe of electron-on-helium physics, enabling the observation of the Wigner crystal transition and a quantitative study of the temperature-dependent plasmon decay arising from ripplon-induced scattering.

I. INTRODUCTION

Longitudinal collective oscillations of electrons, referred to as plasmons, are fundamental excitations originating from long-range Coulomb interactions in diverse electronic systems, ranging from metallic particles to two-dimensional (2D) electron systems. When these oscillations are spatially confined, they are referred to as localized plasmons. The resulting strong electromagnetic field confinement enhances light–matter interactions, enabling a variety of plasmonic applications. In metallic nanoparticles, electrons oscillate coherently in response to an incident optical field, giving rise to localized surface plasmons [1, 2]. These effects have been exploited for photocatalysis [3], plasmon-assisted photovoltaics [4], photodetection [5], and biosensing [6].

In 2D electron systems in semiconductor materials, plasmons have recently attracted growing interest as carriers of quantum information. The coherent generation and manipulation of plasmon wave packets offers a promising route toward transmitting quantum information over finite distances, as proposed and explored in recent theoretical and experimental studies [7–10]. Such propagating modes could, in principle, be coherently captured and stored in a localized cavity mode, providing a means to interface mobile and stationary quantum exci-

tations. To route quantum information beyond the 2D electron system the ability to convert plasmonic states into photons is required. To achieve this, it is of prime importance to realize the strong-coupling regime—where the coherent coupling rate exceeds the dissipation rates.

However, in both metals and 2D semiconductor systems, plasmonic dissipation losses typically make access to this regime challenging, although a notable exception has been demonstrated using periodic arrays of metal nanoparticles [11], where the enhanced plasmon–photon coupling exceeds the plasmon losses.

In this work, we overcome this limitation by employing floating electrons in vacuum, an intrinsically low-dissipation electronic system that enables strong coupling between localized plasmons and photons. Electrons float in vacuum approximately 10 nm above the liquid helium and form a 2D electron system [12–16]. Owing to the absence of disorder and impurities in this pristine environment, electron scattering—and thus dissipation—is strongly suppressed. This exceptionally clean environment has motivated recent proposals and experiments to use single electrons on helium as qubits [17–21]. Most recently, strong coupling between the orbital state of a single electron on liquid helium and a microwave photon confined in a superconducting resonator has been demonstrated [22]. In addition to single-electron dynamics, plasmons were first detected several decades ago using RF absorption techniques in the 50–200 MHz range [23, 24]. Since then, plasmons have not only been studied for their intrinsic properties [25, 26], but have

* asher.jennings@riken.jp

† e2006k@gmail.com

also been used as a probe to discover the Wigner crystal [24] and to investigate the surface properties of superfluid ^3He [27]. Recently, microwave plasmon spectroscopy in the few-gigahertz range has been demonstrated through electron transport measurements [28]. Here, we demonstrate strong coupling between a plasmon mode of electrons on liquid helium and RF photons confined in an LC resonator (Fig. 1(a)). This plasmon-photon coupling platform offers a high degree of tunability, as the electron density, coupling strength, and temperature can be precisely controlled. Combined with the low dissipation enabled by the pristine electron environment, this allows systematic studies of plasmon-photon interactions, including real-time coherent energy exchange in a regime difficult to access in conventional semiconductor 2D materials. Beyond this, we demonstrate that the LC resonator serves as a sensitive probe of electron-on-helium physics by observing the Wigner crystal transition and determining the temperature dependence of the plasmon decay rate.

II. DEVICE

We realize plasmons of 2D electrons floating on liquid helium confined within a circular area and couple them to the electromagnetic mode of an LC resonator (Fig. 1(a)). To laterally confine the electrons region, we employ a so-called Corbino geometry [29] consisting of two parallel plates. Each plate comprises three concentric electrodes—center, middle, and outer—and we apply DC voltages V_{BC} , V_{BM} , and V_{BO} , to the bottom electrodes respectively, while the electrodes of the top plate are left DC grounded. By adjusting these voltages, the radial extent of the region in which electrons can be stably confined is controlled. A nanofabricated inductor is connected to the top center electrode to form the LC resonator [30]. The separation between the top and bottom plates is $D = 2$ mm. Liquid helium with a thickness of 1 mm fills half of this gap. Electrons are deposited onto the liquid helium surface via thermionic emission [21, 31] and subsequently float approximately 10 nm above the liquid helium surface.

We measure the reflection of an RF signal applied to the top center electrode. Fig. 1(b) shows the equivalent electrical circuit of the measurement setup. The reflection coefficient is given by

$$\Gamma_{\text{ref}} = \frac{Z_l - Z_0}{Z_l + Z_0}, \quad (1)$$

where Z_0 is the characteristic impedance of the transmission line and Z_l is the load impedance which represents the coupled system of the LC resonator and plasmons [32],

$$Z_l = \frac{1}{-i\omega C_c} + \left(\frac{1}{Z_L} + \frac{1}{Z_p} \right)^{-1}. \quad (2)$$

Here $C_c = 0.3$ pF is the coupling capacitor and $i = \sqrt{-1}$. The impedance of the parallel LCR circuit is given by $\frac{1}{Z_L} = \frac{1}{R} - i\omega C - \frac{1}{i\omega L}$, while the plasmon impedance Z_p is defined later. The circuit parameters are $L = 708$ nH, $C = 2.131$ pF, and $R = 321$ k Ω . The resonance frequency is $\omega_0/2\pi = 1/2\pi\sqrt{LC_t} = 120.946$ MHz, where $C_t = C + C_c$. The device used here is identical to that reported in Ref. 30, where further circuit details are provided. Within the framework of input–output theory, Eq. (1) can be rewritten as (Supplementary Information B)

$$\Gamma_{\text{ref}} = 1 - \frac{-i\kappa_{\text{ext}}}{(\omega_0 - \omega) - i\frac{\kappa_{\text{ext}} + \kappa_{\text{int}}}{2} + \frac{g^2}{(\omega - \omega_p) + i\gamma_p/2}}, \quad (3)$$

where ω_p is the angular frequency of the plasmon mode, g is the coupling strength between the resonator and the plasmon mode, $\kappa_{\text{ext}}/2\pi = 0.19$ MHz and $\kappa_{\text{int}}/2\pi = 0.20$ MHz are the external and internal decay rates of the resonator, respectively, and γ_p is the decay rate of the plasmon mode. In the absence of electrons ($g = 0$), Eq. (3) reduces to the standard expression for a single-port resonator. The corresponding measured reflection coefficient is shown in Fig. 1(c).

III. FREQUENCY-DOMAIN MEASUREMENT

The radial component of the RF field induced by the incident signal on the top center electrode drives charge-density oscillations in the electron layer (Fig. 1(a)). This leads to coupling between the confined plasmon mode and the resonator field when the plasmon mode frequency ω_p approaches the resonator frequency ω_0 . The angular frequency of a 2D plasmon mode for a uniform electron density confined between the top and bottom electrodes, is given by [26, 33]

$$\omega_p = \sqrt{\frac{e^2 n_0 k_{\nu,\mu}}{2 m_e \epsilon_0} \tanh\left(\frac{k_{\nu,\mu} D}{2}\right)}, \quad (4)$$

where e is the elementary charge, n_0 is the 2D electron density, m_e denotes the free electron mass, ϵ_0 is the vacuum permittivity. Here the relative permittivity of liquid helium is approximated as $\epsilon_r = 1$. The quantity $k_{\nu,\mu}$ represents the wave number of the plasmon mode characterized by the azimuthal mode index ν and the radial mode index μ in the cylindrical geometry. Due to our device geometry, only radial modes are efficiently driven; therefore, we consider only the fundamental azimuthal mode ($\nu = 0$). Note that the wave number $k_{0,\mu}$ is determined by the boundary condition at the edge of the circular electron sheet and therefore depends on its radius.

To prepare electrons on the helium surface, we first set a positive voltage to all the bottom electrodes $V_{\text{BC}} = V_{\text{BM}} = V_{\text{BO}} > 0$. Electrons are then deposited onto the helium surface until the saturation density is reached,

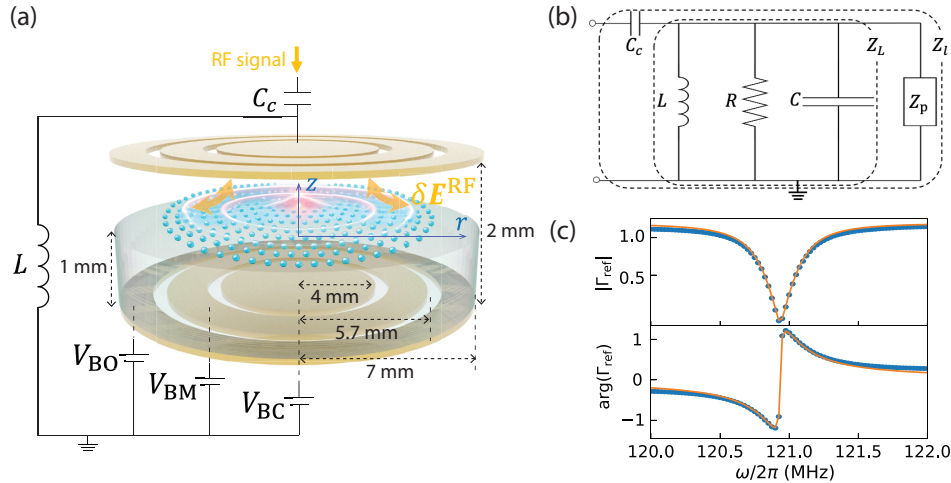


FIG. 1. (a) Experimental setup with Corbino-geometry electrodes forming part of an LC resonator. The device consists of radially arranged top and bottom electrodes, each with an area of approximately 0.5 cm^2 , which form the main capacitance C of the LC resonator. The top center electrode is connected to an inductor L , which provides the resonant inductance, and to a coupling capacitor C_c that interfaces the resonator with the external circuit. The bottom electrodes are immersed in a 1-mm-thick layer of liquid helium (light blue cylinder), above whose surface electrons (light blue circles) float approximately 10 nm in vacuum. An RF signal applied to the top center electrode generates an oscillating radial electric field δE_r^{RF} confined within the LC resonator and drives collective electron oscillations (plasmon mode, schematically illustrated by the pink wave) in electrons on helium. (b) Schematic representation of the experimental setup in the form of an equivalent electrical circuit. The plasmon excitation is modeled by an effective impedance Z_p . Further details regarding the circuit elements are provided in the main text. (c) Measured magnitude and phase of the reflection coefficient of the LC resonant circuit, $|\Gamma_{\text{ref}}|$ and $\arg(\Gamma_{\text{ref}})$, in the absence of electrons (blue dots). The orange lines show a fit to Eq. (3) with $g = 0$. The data shown here are corrected for the phase offset and cable delay and are normalized, as is the case for all reflection data presented in this manuscript.

corresponding to the maximum electron density allowed for the given V_{BC} . We confine the electrons primarily to the center electrode by first sweeping the outer electrode to $V_{\text{BO}} = -32 \text{ V}$, and then the middle electrode $V_{\text{BM}} = -32 \text{ V}$.

In frequency-domain measurements, the plasmon frequency ω_p is tuned by simultaneously adjusting the electron density n_0 and the wave vector $k_{0,\mu}$ (see Eq. 4). V_{BM} was subsequently swept between -32 V and 5 V while keeping V_{BO} and V_{BC} constant.

The measured reflection coefficient is shown in Fig. 2(a) for several different values of V_{BC} (i.e., several different saturation densities). When ω_p is tuned into resonance with the LC resonator ($\omega_p = \omega_0$), an avoided level crossing appears. The electron density profiles for several values of V_{BM} at fixed $V_{\text{BC}} = 7.5 \text{ V}$ and $V_{\text{BO}} = -32 \text{ V}$ are shown in Fig. 2(b). These profiles are obtained by solving the Poisson equation for the actual device geometry, using the applied voltages V_{BO} , V_{BM} , and V_{BC} as input parameters [34] (see Refs. 30 and 35 for details of the numerical procedure). During this V_{BM} sweep, the electron pool radius and the electron density n_0 are varied simultaneously while keeping the total number of electrons fixed, thereby tuning ω_p . As seen in Fig. 2(a) for $V_{\text{BC}} = 7.5 \text{ V}$, avoided crossings occur at $V_{\text{BM}}^{\text{exp}} = -26.4 \text{ V}$ and 0.8 V . These avoided crossings occur when the plasmon frequencies ω_p of the fundamental and second modes are tuned to the resonator frequency ω_0 , respec-

tively, as determined from the ω_p calculations using the procedure described below.

For a quick estimate of ω_p , we adopt the following approximation. We model the electron sheet as a disk of uniform electron density n_0 with an effective radius R^* . The radius R^* is defined as the radius at which the simulated density drops to zero, and n_0 is chosen such that the total number of electrons in the disk is equal to that obtained from the simulated density profile. The wave number $k_{0,\mu}$ is determined by the boundary condition that the radial current vanishes at R^* , which is given by $J'_0(k_{0,\mu} R^*) = 0$, where J'_0 denotes the derivative of the zeroth-order Bessel function [26] (see Supplementary Information A). Using this approximation, we obtain a fundamental ($\mu = 1$) plasmon frequency of $\omega_p/2\pi = 125.0 \text{ MHz}$ for $V_{\text{BC}} = 7.5 \text{ V}$ and $V_{\text{BM}}^{\text{exp}} = -26.4 \text{ V}$. We therefore attribute the observed avoided crossing at this bias point to the fundamental plasmon mode being tuned into resonance with the LC resonator. The deviation from ω_0 can be attributed to the uniform-density approximation, which neglects the gradual decrease of the electron density near the edge of the electron sheet (Supplementary Information A). The second mode ($\mu = 2$) plasmon frequency at the avoided crossing observed at $V_{\text{BM}}^{\text{exp}} = 0.8 \text{ V}$ is estimated to be $\omega_p/2\pi \simeq 130.5 \text{ MHz}$, which is noticeably higher than the bare resonator frequency $\omega_0/2\pi$. A definitive mode assignment cannot be made from this quick estimate alone. As discussed be-

low, a more accurate evaluation shows that this feature indeed originates from the second plasmon mode.

A more accurate estimate of ω_p is obtained by treating them as the eigenvalues of a self-consistent charge-density equation derived from the continuity equation and Coulomb interactions (see Ref. 34 and Sec. VII A in Methods), using only the simulated density profiles as input. The resulting plasmon frequencies for the first through fourth radial modes are shown in Fig. 2(c) as dashed lines (blue, orange, green, and light blue). Fig. 2(d) shows the electron density profiles when the fundamental plasmon mode frequency is tuned to the resonator frequency for four different values of V_{BC} . This approach also yields the plasmon impedance Z_p , defined through the charge variation δQ induced on the top center electrode by the plasmonic density oscillation, quantifying how the plasmon mode couples to the resonator (Sec. VII A in Methods). The simulation results of the reflection coefficient, calculated using Eq. 2 with the corresponding plasmon impedance Z_p , are shown in Fig. 2(c). For the reflection-coefficient simulations, the plasmon relaxation rate γ_p is included as an additional input parameter and its value is extracted from the experimental data (Supplementary Information B). The simulation results in Fig. 2(c) are in good agreement with the experimental data in Fig. 2(a), both in the resonance positions and in the coupling strength between the LC resonator field and the plasmon mode. A comparison of these two figures shows, for example, that the observed avoided crossing at $V_{BC} = 7.5$ V and $V_{BM}^{\text{exp}} = 0.8$ V in Fig. 2(a) can be attributed to the second ($\mu = 2$) plasmon mode being tuned into resonance with the LC resonator.

The remaining deviations between experiment and simulation, particularly for positive V_{BM} , may arise from geometrical elements not included in the simulation, e.g., the gap between the electrodes. The magnitude of the density modulation for the first, second, and third radial plasmon modes, $|\delta n(r)|$, evaluated at resonance, is shown in Fig. 2(e). The number and positions of the nodes directly illustrate how standing waves are formed in each radial mode.

IV. STRONG COUPLING AND TIME-DOMAIN DYNAMICS

To enhance the coupling strength g and enter the strong-coupling regime, we populate electrons above both the bottom-center and bottom-middle electrodes by setting $V_{BC} = V_{BM} = 17$ V while applying a negative bias V_{BO} . This configuration extends the electron cloud toward the outer region of the top-center electrode ($r \simeq 4$ mm), where the radial RF electric field δE_r^{RF} is strongest. As a result, the spatial overlap between the plasmon current and the resonator field is enhanced, thereby increasing the coupling strength g (Supplementary Information C).

In this experiment, V_{BO} is swept, rather than V_{BM} , to

tune ω_p . Fig. 3(a) shows the reflected signal as a function of V_{BO} . At $V_{BO} = -29$ V, where the plasmon mode is tuned into resonance with the LC resonator, a clear splitting of the resonance peak is observed, indicating hybridization between the plasmon and resonator modes. Fitting the spectrum with Eq. (3) yields $g/2\pi = 4.55 \pm 0.02$ MHz and $\gamma_p/2\pi = 5.10 \pm 0.07$ MHz (Supplementary Information B). The mode splitting at resonance is given by $2\Lambda_0$ (Supplementary Information B), where

$$\Lambda_0 = \sqrt{g^2 - \left(\frac{\Delta_\kappa}{4}\right)^2}, \quad (5)$$

with $\Delta_\kappa = \kappa - \gamma_p$. $\kappa/2\pi = (\kappa_{\text{int}} + \kappa_{\text{ext}})/2\pi = 0.39$ MHz is the total resonator decay rate. The observation of a real-valued Λ_0 and the associated peak splitting is a hallmark of the strong-coupling regime. The corresponding simulation is shown in Fig. 3(b) and exhibits good agreement with the measured spectrum in terms of both the resonance position and the coupling strength.

Furthermore, to directly probe the dynamical coupling between the LC resonator and the plasmon mode, we performed time-domain microwave reflectometry measurements. A 20 ns RF pulse was injected into the resonator, and the reflected signal was demodulated into its in-phase (I) and quadrature (Q) components (Supplementary Information VII B). After the incident pulse is switched off, the detected power $I^2(t) + Q^2(t)$ is proportional to the energy stored in the resonator, $|a(t)|^2$, during the ring-down, where $|a(t)|$ denotes the intracavity field amplitude. The reflected signal is recorded as a function of time and V_{BO} , demonstrating clear oscillatory dynamics corresponding to time-domain energy exchange between the plasmon mode and RF photons. These dynamics manifest as Rabi-like oscillations [36, 37], i.e., classical normal-mode beating, and are most pronounced near zero-detuning ($V_{BO} = -29$ V in Fig. 3(c)). On resonance, the energy stored in the resonator exhibits a decaying oscillation:

$$|a(t)|^2 \propto e^{-\frac{\Sigma_\kappa}{2}t} \cos^2(\Lambda_0 t + \phi), \quad (6)$$

where $\Sigma_\kappa = \kappa + \gamma_p$ and Λ_0 is the oscillation frequency given by Eq. 5 (Sec. VII C in Methods). By fitting this expression to the measured $I^2 + Q^2$ trace at $V_{BO} = -29$ V where $\Delta \approx 0$, we extract $g/2\pi = 4.906 \pm 0.009$ MHz and $\gamma_p/2\pi = 3.30 \pm 0.02$ MHz (inset of Fig. 3(c)). These values slightly differ from those obtained in the frequency-domain measurements ($g/2\pi = 4.55 \pm 0.02$ MHz and $\gamma_p/2\pi = 5.10 \pm 0.07$ MHz). This discrepancy may arise because, during the time-domain experiment, no continuous RF power is applied to the device, which can lead to decreases in the electron temperature and thereby modify the effective coupling and dissipation mechanisms (Supplementary Information D). The calculated time-domain response shown in Fig. 3(d) reproduces the main features of the experimental data. Off resonance, the decay is governed by the resonator decay rate κ , while on resonance

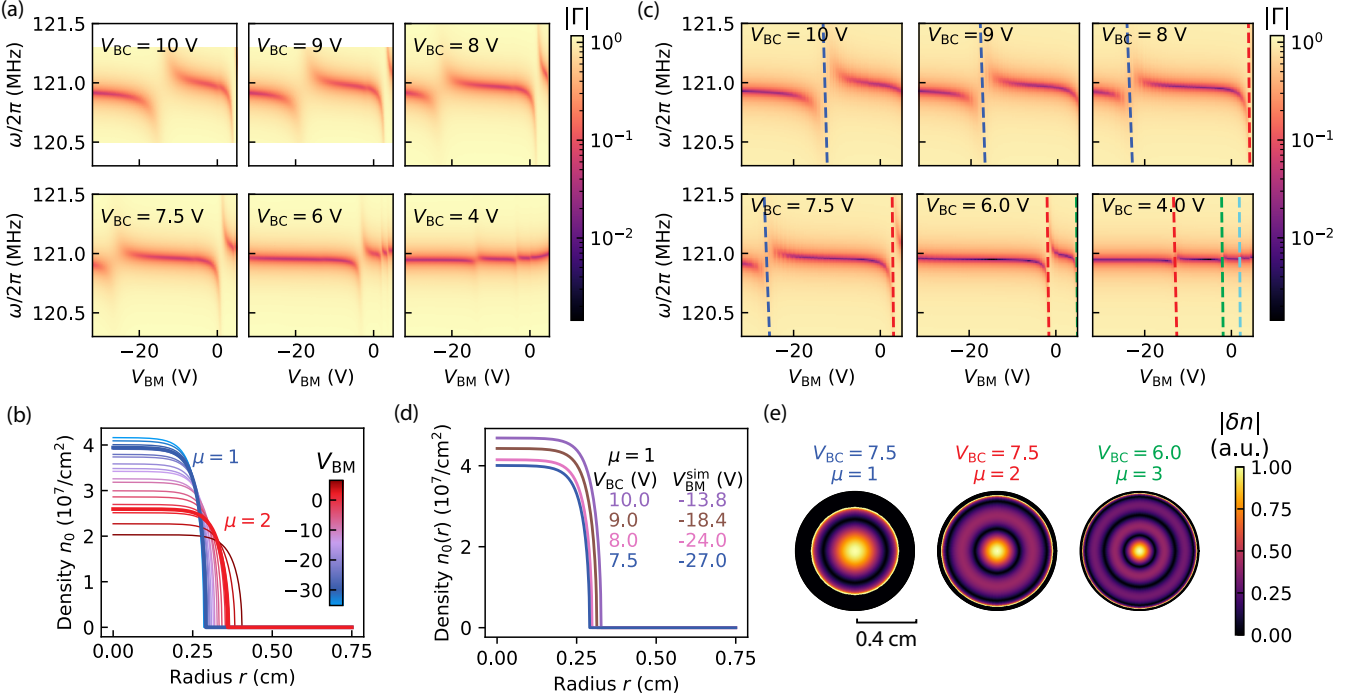


FIG. 2. Magnitude of the reflection coefficient $|\Gamma|$ as a function of V_{BM} and RF signal frequency $\omega/2\pi$ from both experiment in (a) and simulation in (c) for different $V_{BC} = 10, 9, 8, 7.5, 6, 4$ V. V_{BO} is fixed to -32 V. (a) Measurement temperature $T = 180$ mK; The RF excitation power is set to -50 dBm at the output of the signal generator. (b) Simulated electron density profiles $n_0(r)$ for different values of V_{BM} , with V_{BC} fixed at 7.5 V and V_{BO} fixed at -32 V. For all values of V_{BM} , the total number of electrons is kept constant. The thick blue and red lines correspond to the density profiles for which the fundamental and second plasmon modes, respectively, are tuned into resonance with the LC resonator frequency according to the simulation shown in (c). (c) Simulated magnitude of the reflection coefficient. Overlaid dashed lines indicate the calculated plasmon-mode frequencies: the fundamental ($\mu = 1$, blue), second ($\mu = 2$, red), third ($\mu = 3$, green), and fourth ($\mu = 4$, light blue) modes. (d) Simulated electron density profiles $n_0(r)$ for $V_{BC} = 10, 9, 8$, and 7.5 V, evaluated at V_{BM}^{sim} where the fundamental plasmon mode ($\mu = 1$) is resonant with the LC resonator according to the simulation shown in (c). (e) Simulated magnitude of the density modulation, $|\delta n|$, at resonance for the fundamental ($\mu = 1$) and second ($\mu = 2$) modes at $V_{BC} = 7.5$ V, and for the third mode ($\mu = 3$) at $V_{BC} = 6$ V. The plasmon decay rates used in the simulations can be found in Supplementary Information B, Fig. 5.

(zero detuning) it is given by $(\kappa + \gamma_p)/2$ due to hybridization with the plasmon mode. Because $\gamma_p > \kappa$, the decay is slower in the off-resonant regime. At the same time, for finite detuning $\Delta = \omega_0 - \omega_p$ in the off-resonant regime, the oscillation frequency increases to $\Lambda \approx \sqrt{g^2 + (\frac{\Delta}{2})^2}$, resulting in faster oscillations than on resonance.

V. TEMPERATURE-DEPENDENT PLASMON DECAY RATE AND WIGNER CRYSTAL TRANSITION

Under the same voltage configurations that satisfies the strong-coupling condition discussed in the previous section, we increased the temperature and observed that the resonance split peaks gradually disappeared (Fig. 4 (a)). The disappearance of the split peaks at higher temperatures results from the increase of the plasmon decay rate γ_p , which violates the strong-coupling condition requiring Λ_0 to be real. Note that this effect is

not caused by electron loss. If the electrons were absent, the resonance peak should be a sharp single peak characterized only by the decay rate of the LC resonator, $\kappa/2\pi = 0.39$ MHz. In contrast, at elevated temperatures the linewidth is governed by the much larger plasmon decay rate γ_p , confirming that the peak merging originates from enhanced plasmon decay. We fitted the temperature-dependent resonance peaks at each temperature using Eq. 3 and extracted the plasmon decay rate γ_p (Fig. 4 (b)), the detuning $\Delta = \omega_0 - \omega_p$ (Fig. 4 (c)), and the coupling strength g (Fig. 4(d)).

Plasmon decay is related to electron scattering via $\gamma_p = 1/\tau$, where τ denotes the electron momentum-relaxation time. For electrons on helium, τ is governed by electron-riplpon and electron-helium vapor scattering: ripplons are quantized surface waves of liquid helium, and thermally populated long-wavelength ripplon modes dominate below 700 mK for the pressing field used here, while scattering by helium vapor atoms becomes the main relaxation mechanism above 700 mK [14, 38]. These processes determine the temperature dependence

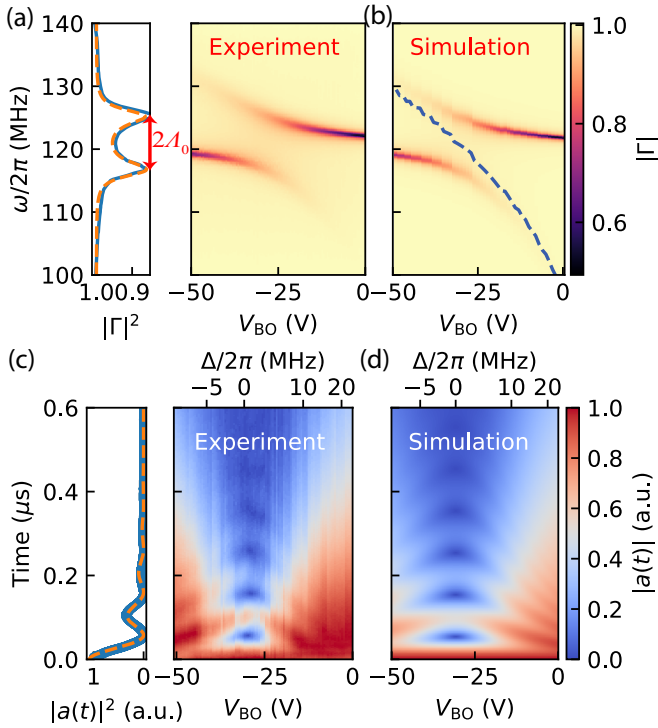


FIG. 3. (a,c) Measurement temperature $T = 180$ mK; The RF excitation power is set to -20 dBm at the output of the signal generator. (a) Right: Normalized measured reflection coefficient as a function of the bottom outer electrode voltage V_{BO} and the RF frequency applied to the LC resonator. The other electrode voltages are fixed at $V_{BC} = V_{BM} = 17$ V. An avoided crossing is observed when the plasmon frequency is tuned into resonance with the LC circuit, indicating coherent coupling between the two modes. Left: Reflection spectrum at the resonance point $V_{BO} = -29$ V (blue solid line), together with a fit to Eq. 3 (orange dashed line). The fit yields a coupling strength $g/2\pi = 4.55 \pm 0.02$ MHz and a plasmon decay rate $\gamma_p/2\pi = 5.10 \pm 0.07$ MHz. From these parameters, we obtain a mode splitting $2\Lambda_0 \approx 9.0$ MHz (Eq. 5). (b) Numerically simulated reflection coefficient corresponding to panel (a). The plasmon decay rate $\gamma_p/2\pi = 5.1$ MHz is used as an input parameter for the simulation. At the resonance voltage $V_{BO} = -30.7$ V, fitting the simulated spectrum yields $g/2\pi = 4.55$ MHz, consistent with the experiment. The overlaid dashed blue lines indicate the calculated fundamental plasmon mode frequencies. (c) Measured $\sqrt{I^2 + Q^2}$ of the reflected signal following a 20 ns RF pulse. Inset: Time-resolved $I^2 + Q^2$ response measured at the resonance point $V_{BO} = -29$ V (blue dots). The orange dashed line shows a fit to Eq. 6, up to an overall proportionality constant, yielding $g/2\pi = 4.906 \pm 0.009$ MHz and $\gamma_p/2\pi = 3.30 \pm 0.02$ MHz. (d) Analytical calculation corresponding to panel (c), performed with the resonance point set to $V_{BO} = -29$ V. The color scale represents the amplitude of the RF field stored in the LC resonator, $|a(t)|$, calculated using Eq. 24 with $g/2\pi = 4.9$ MHz, $\gamma_p/2\pi = 3.3$ MHz, and $\kappa/2\pi = 0.39$ MHz. (c,d) The detuning on the upper horizontal axis, $\Delta = \omega_0 - \omega_p$, is obtained from the numerically calculated relation between V_{BO} and ω_p .

of τ , and hence of γ_p . The measured plasmon decay rate

γ_p agrees well with theoretical calculations neglecting many-electron effects in the zero-frequency (DC) limit for an effective pressing field of 92 V/cm [39], obtained from V_{BC}/D with a correction for image-charge fields due to the electrons being located just below the midplane at $0.48D$ [40] (Fig. 4(b)). This temperature dependence is also consistent with previously reported experimental results obtained under comparable pressing-field conditions from low-frequency mobility measurements [27, 41] and plasmon absorption measurements [27]. At the electron density of this experiment ($n \sim 10^8$ cm $^{-2}$), Ref. 41 suggested that many-electron effects begin to emerge in this density regime, although they remain relatively weak [14, 42]. The drop of g observed for $T \gtrsim 700$ mK (Fig. 4(d)) is likely due to a partial loss of electrons. In the same temperature range, the apparent reduction of γ_p can be attributed to a decrease in the number of electrons participating in the collective plasmon mode, together with an increased uncertainty in the fitting procedure.

The detuning Δ shows a pronounced change around 250 mK. This behavior is associated with a rapid change in the plasmon frequency ω_p due to the formation of a Wigner crystal. Below this temperature, the electrons are expected to crystallize into the Wigner crystal phase, whereas above it they remain in the liquid phase. For temperature $T \approx 250$ mK and 2D electron density of $n_0 \approx 10^8$ cm $^{-2}$, the 2D plasma parameter (also referred to as the Coulomb coupling parameter) is estimated as

$$\Gamma = \frac{e^2}{4\pi\epsilon_0 k_B T} \sqrt{\pi n_0} \approx 120,$$

which is consistent with previously reported values [14, 15, 43–45]. In this regime, the periodic electron lattice induces a commensurate deformation of the helium surface called the dimple sublattice, leading to stronger coupling between plasmons and ripplons. As a consequence, multiple branches of coupled plasmon-ripple modes emerge. The highest-frequency branch, referred to as the optical branch, has a frequency $\sqrt{\omega_p^2 + \omega_d^2}$, where ω_d denotes the frequency of electrons oscillating in the local dimple potential, which we refer to as the dimple frequency. With decreasing temperature, the dimple potential deepens and ω_d increases toward its zero-temperature value $\omega_d^0 = 75$ MHz for a pressing field of 92 V/cm [14]. As a result, the optical mode frequency becomes higher and the detuning Δ shifts from its value in the electron fluid phase. From the observed $\Delta = 2$ MHz at our lowest temperature (167 mK), we evaluate the dimple frequency to be $\omega_d/2\pi = 29$ MHz, consistent with the above picture.

In contrast, no clear signature of Wigner crystallization is observed in the plasmon decay rate γ_p . This is consistent with earlier work [27], which showed that the plasmon linewidth measured using absorption spectroscopy remains insensitive to Wigner crystallization, whereas the mobility measured at low-frequency ($\lesssim 1$ MHz) exhibits a rapid decrease. This difference originates from

the distinct probe-frequency regimes. At low frequencies, the motion of the Wigner crystal drags the dimple sublattice along at the same velocity, which effectively increases the electron mass m_e by the dimple mass M_d ($M_d/m_e \sim$ several hundred). This large mass enhancement renders the inertia term non-negligible at lower frequencies ($\lesssim 1$ MHz), resulting in a significant reduction of the mobility in the Wigner crystal phase [46]. In contrast, in the optical branch, the Wigner crystal and the dimple sublattice oscillate 180° out of phase. Because of the large mass difference between m_e and M_d , the dimple sublattice remains nearly stationary, and the electrons oscillate with only a small amplitude around the bottoms of the dimples. In this regime, theoretical studies [14, 47] indicate that the scattering rate is nearly the same in the Wigner crystal and electron liquid phases, and that there is no significant difference between the zero- and high-frequency scattering rates, except at very low temperatures ($k_B T < \hbar\omega$), where k_B is the Boltzmann constant and \hbar is Planck's constant. These predictions are consistent with our observations in Fig. 4(b).

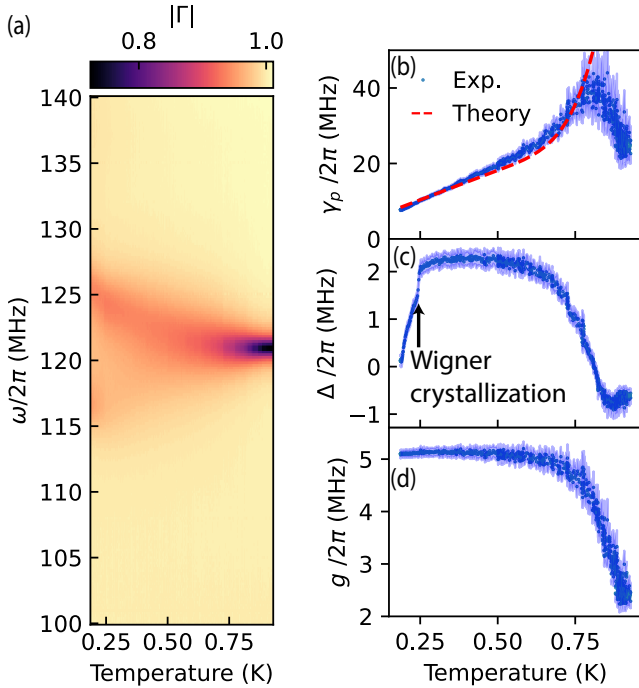


FIG. 4. The RF excitation power is set to -50 dBm at the output of the signal generator. (a) Resonance peaks measured at $V_{BO} = -29$ V as a function of temperature; other measurement conditions are identical to those in Fig. 3(a). (b,c,d) Temperature dependence of the plasmon decay rate γ_p in (b), the detuning $\Delta = \omega_0 - \omega_p$ in (c), and the coupling strength g in (d), obtained from fit of Eq. 3 to the data in (a). Blue circles represent the extracted values, while the semi-transparent blue lines indicate the fitting uncertainties (95% confidence intervals, as used throughout this manuscript). In (b), the red dashed line shows $\gamma_p = 1/\tau$, where τ is the momentum-relaxation time calculated using the theoretical model reported in Ref. 39 for a pressing field of 92 V/cm.

VI. CONCLUSION AND OUTLOOK

We demonstrate the hybridization of RF electromagnetic fields and plasmons of electrons on liquid helium. By tuning the DC voltages applied to the electrodes beneath the electron layer, both the plasmon frequency and the coupling strength can be controlled. The excellent agreement between experiment and theoretical calculations highlights the purity of the electron-on-helium system, which enables accurate modeling and quantitative simulation of the coupled dynamics. The LC resonator-based plasmon readout technique also provides a useful means to study electron dynamics on helium such as the Wigner crystal transition and the temperature-dependent electron scattering process.

The demonstration of strong coupling between plasmons and an LC resonator reported here constitutes an important step toward using plasmons as carriers of quantum information. In the present work, the plasmon frequency $\omega_p/2\pi \approx 120$ MHz lies below the thermal energy $k_B T/h$ at the operating temperature of $T \approx 180$ mK. Under these conditions, thermal noise is expected to dominate, rendering plasmons unsuitable for storing quantum information. A natural next step is therefore to confine plasmons to smaller spatial regions to increase their frequency into the gigahertz range. Plasmon modes in the 4–8 GHz range have already been demonstrated for electrons on helium, matching the operating frequencies of superconducting resonators [18, 28]. Achieving strong coupling in this frequency range would enable operation in the quantum regime, where plasmons can coherently exchange quantum information with a microwave photon in a superconducting resonator.

VII. METHODS

A. Simulation of the plasmon frequency and impedance

In this section, we describe how the plasmon frequencies (dashed lines in Fig. 2(c)) and the plasmon impedance Z_p used to calculate the reflection coefficient Γ in Fig. 2(c) are obtained. The calculation is based on a self-consistent charge-density equation derived from the continuity equation and Coulomb interactions, which is solved using only the simulated electron density profiles as input.

Plasmon frequency

Charge conservation in the 2D electron system is described by the continuity equation, which relates the time derivative of the charge density to the current flow. Assuming azimuthal symmetry in cylindrical coordinates,

the continuity equation for the electron sheet reads

$$-e \frac{\partial n(r, t)}{\partial t} + \frac{1}{r} \frac{\partial}{\partial r} [r j_r(r, t)] = 0, \quad (7)$$

where $n(r, t) = n^0(r) + \delta n(r, t)$. Here, $n^0(r)$ is the static electron density profile, as shown in Fig. 2(b,d), and $\delta n(r, t)$ denotes the oscillating electron density fluctuation. The RF voltage $ve^{-i\omega t}$ applied to the top center electrode acts as the external excitation, generating an oscillating electric field $\delta \mathbf{E}^{\text{RF}}(r, t) = \delta E_r^{\text{RF}}(r, t) \mathbf{r} + \delta E_z^{\text{RF}}(r, t) \mathbf{z}$ in the electron layer and inducing plasmonic charge motion. Owing to the cylindrical symmetry of the excitation, the electric field has only r and z components, while the current density is purely radial and confined to the 2D electron sheet. The radial current density depends linearly on the local electric field and is given by

$$j_r(r, t) = \sigma(r) \delta E_r(r, t), \quad (8)$$

where the 2D conductivity is

$$\sigma(r) = \frac{e^2 n^0(r) \tau}{m} \frac{1}{1 - i\omega\tau}. \quad (9)$$

The oscillating electric field consists of the externally applied RF component and the self-consistent field generated by electron density fluctuations,

$$\delta E_r(r, t) = \delta E_r^{\text{RF}}(r, t) + \delta E_r^{\text{pl}}(r, t). \quad (10)$$

Correspondingly, the radial current density can be decomposed into an externally driven component and a plasmon-induced component,

$$j_r(r, t) = j_r^{\text{RF}}(r, t) + j_r^{\text{pl}}(r, t), \quad (11)$$

with

$$j_r^{\text{RF}}(r, t) = \sigma(r) \delta E_r^{\text{RF}}(r, t), \quad (12)$$

$$j_r^{\text{pl}}(r, t) = \sigma(r) \delta E_r^{\text{pl}}(r, t). \quad (13)$$

The plasmon-induced component δE_r^{pl} represents the self-consistent internal restoring field arising from Coulomb interactions between electrons [34, 48]. It is given by

$$\delta E_r^{\text{pl}}(r, t) = - \int dr' \delta n(r', t) \partial_r G(r, r'), \quad (14)$$

where $\partial_r G(r, r')$ is the radial derivative of the Green's function describing the electric field at radius r generated by a unit charge fluctuation at r' . This internal field acts as a restoring field: any spatial modulation of the electron density produces a charge imbalance that generates an electric field tending to suppress the modulation, giving rise to collective plasmon oscillations. Taking $\delta n(r, t) = \delta n(r) e^{-i\omega t}$ (and similarly for fields and currents), Eq. (7) becomes

$$i\omega e \delta n(r) + \frac{1}{r} \frac{\partial}{\partial r} [r \sigma(r) (\delta E_r^{\text{RF}}(r) + \delta E_r^{\text{pl}}(r))] = 0. \quad (15)$$

Substituting the plasmon-induced electric field (Eq. (14)) into the frequency-domain continuity equation (Eq. (15)) yields an integral equation for the oscillating electron density $\delta n(r)$,

$$\int dr' \mathcal{H}(r, r'; \omega) \delta n(r') = \frac{1}{r} \frac{\partial}{\partial r} [r \sigma(r) \delta E_r^{\text{RF}}(r)], \quad (16)$$

where $\mathcal{H}(r, r'; \omega)$ is a linear kernel determined by the device geometry through the Green's function $G(r, r')$, the static electron density profile $n^0(r)$ through the conductivity $\sigma(r)$, and the angular frequency ω . In the absence of external RF driving, $\delta E_r^{\text{RF}}(r) = 0$, Eq. (16) reduces to the homogeneous integral equation

$$\int dr' \mathcal{H}(r, r'; \omega) \delta n(r') = 0. \quad (17)$$

Nontrivial solutions of Eq. (17) exist only for discrete values of ω , which define the plasmon frequencies [48]. Each such eigenfrequency is associated with an eigenfunction $\delta n(r)$ describing a standing-wave charge-density oscillation in the radial direction. These solutions correspond to the μ -th radial plasmon modes, $\mu = 1, 2, 3, \dots$

Plasmon impedance

When an AC voltage $ve^{-i\omega t}$ is applied to the top center electrode, it generates a radial RF electric field $\delta E_r^{\text{RF}}(r)$. According to Eq. (16), this RF field modulates the electron density, resulting in a density variation $\delta n(r)$. This density modulation induces a charge variation δQ on the top center electrode [34]. The coupling between the LC resonator and the plasmon mode arises from this density-induced charge on the top center electrode. The resulting plasmon impedance is given by [32]

$$Z_p = \frac{v}{-i\omega(\alpha \delta Q)}. \quad (18)$$

Here, we introduce a factor α to account for the real device, in which a fraction of the induced image charge is shunted into parasitic capacitances, mainly originating from metal plates on the back side of the PCB that are not included in the simulation. We define a participation ratio $\alpha = C_{\text{sim}}/C$, where C_{sim} is the capacitance obtained from the simulated geometry and C is the capacitance of the real device including parasitic contributions. The latter is extracted as $C = 2.131 \text{ pF}$ by fitting Eq. B1 to the measured resonance peak, using an independently measured inductance L [30]. With $C_{\text{sim}} = 0.5 \text{ pF}$, we obtain $\alpha \approx 0.25$. As a result, the effective charge contributing to the plasmon response is reduced from δQ to $\alpha \delta Q$, as reflected in Eq. (18).

In Fig. 2(a,c), the experimentally extracted coupling strengths are slightly larger than the simulated values, which may reflect minor geometric features of the actual device—such as conducting support structures and exposed 0.1 mm dielectric regions between electrodes—that are not fully captured in the simulation.

The continuous formulation described above is implemented numerically by discretizing the system in cylindrical coordinates (r, z) . For the simulations corresponding to Fig. 2 and Fig. 3, the radial coordinate is discretized over $0 \leq r \leq 7.5$ mm and the vertical coordinate is discretized over $-1 \text{ mm} \leq z \leq 1 \text{ mm}$. The radial direction is divided into 500 grid points, while the z direction is divided into 200 grid points. All numerical calculations are performed in Python. The codes can be found in Ref. 49. The only input parameters of the numerical simulation are the static electron density profile $n^0(r)$ and the electron momentum-relaxation time τ ; no additional free parameters are introduced.

B. Time-domain measurement

A time-domain microwave reflectometry measurement was performed to probe the plasmon dynamics. Two microwave sources (Keysight E8267D and Rohde & Schwarz SMB100A) were phase-locked to a common 10 MHz reference provided by a Stanford Research Systems FS725 rubidium frequency standard. Microwave pulses with a duration of 20 ns were generated using a Tektronix AWG 5204. A Kaiser–Bessel envelope with $\beta = 14$ was employed to suppress spectral leakage and unwanted frequency components. The pulse waveform was fed into the I port of the internal IQ modulation mode of a Keysight E8267D, generating RF pulses with a source power of -20 dBm. Before reaching port 1 of the sample, the signal was attenuated by a total of 38 dB in the input line inside the refrigerator, including all inserted attenuators. The reflected signal from port 2 of the sample was amplified first at 4 K by $+40$ dB using a Cosmic Microwave Technology CITLF3 cryogenic amplifier, further amplified at room temperature by 20 dB using a Mini-Circuits ZFL-500LN+ low-noise amplifier. The signal subsequently demodulated using a Polyphase Quadrature Demodulator (AD0105B), with the Rohde & Schwarz SMB100A serving as the local oscillator reference. The in-phase (I) and quadrature (Q) voltage components were passed through a Mini-Circuits SLP-50+ low-pass filter and recorded by a Teledyne LeCroy WaveRunner 9054 oscilloscope (500 MHz bandwidth), with 200 waveform averages performed in real time. To remove systematic distortion of the demodulator response (including I/Q gain imbalance, phase offsets, and DC offsets), a full complex calibration of the demodulation chain was implemented in software.

The detected power satisfies

$$I^2(t) + Q^2(t) \propto |a_{\text{out}}(t)|^2,$$

where $a_{\text{out}}(t)$ is the output field of the resonator. The resonator input–output relation is

$$a_{\text{out}}(t) = a_{\text{in}}(t) - \sqrt{\kappa_{\text{ext}}} a(t),$$

where $a_{\text{in}}(t)$ denotes the incident field at the resonator.

After the incident field is switched off, $a_{\text{in}}(t) \approx 0$, so that

$$a_{\text{out}}(t) \approx -\sqrt{\kappa_{\text{ext}}} a(t), \quad |a_{\text{out}}(t)|^2 \propto |a(t)|^2.$$

Thus, in the ring-down regime, the measured IQ power $I^2(t) + Q^2(t)$ is directly proportional to the energy stored in the resonator, i.e., the intracavity photon number $|a(t)|^2$.

C. Time-domain coupled-mode

The equations of motion for the coupled LC resonator mode $a(t)$ and the plasmon mode $b(t)$ are

$$\frac{d}{dt} \begin{pmatrix} a \\ b \end{pmatrix} = \begin{pmatrix} -\kappa/2 - i\omega_0 & -ig \\ -ig & -\gamma_p/2 - i\omega_p \end{pmatrix} \begin{pmatrix} a \\ b \end{pmatrix}, \quad (19)$$

where κ and γ_p denote the decay rates of the two modes. The eigenvalues of this dynamical matrix are $-i\tilde{\omega}_{\pm}$ where

$$\tilde{\omega}_{\pm} = \omega_0 - \frac{\Delta}{2} - i\frac{\Sigma_{\kappa}}{4} \pm \Lambda. \quad (20)$$

where

$$\Lambda = \sqrt{\left(\frac{\Delta}{2} - i\frac{\Delta_{\kappa}}{4}\right)^2 + g^2}, \quad (21)$$

$\Sigma_{\kappa} = \kappa + \gamma_p$, $\Delta_{\kappa} = \kappa - \gamma_p$, and the detuning is defined as $\Delta = \omega_0 - \omega_p$. For the initial condition $a(0) = 1$ and $b(0) = 0$, the mode amplitudes can be written as a superposition of the two normal modes,

$$a(t) = A e^{-i\tilde{\omega}_{+}t} + (1 - A) e^{-i\tilde{\omega}_{-}t}, \quad (22)$$

$$b(t) = \alpha_{+} A e^{-i\tilde{\omega}_{+}t} + \alpha_{-} (1 - A) e^{-i\tilde{\omega}_{-}t}, \quad (23)$$

with $\alpha_{\pm} = \frac{-\frac{\Delta}{2} + i\frac{\Delta_{\kappa}}{4} \pm \Lambda}{g}$ and $A = \frac{1}{2} \left(1 + \frac{\frac{\Delta}{2} - i\frac{\Delta_{\kappa}}{4}}{\Lambda} \right)$. The resulting cavity-field amplitude is therefore given by

$$|a(t)| = e^{-\frac{\Sigma_{\kappa}}{4}t} |A e^{-i\Lambda t} + (1 - A) e^{i\Lambda t}|, \quad (24)$$

which describes oscillatory energy exchange with an overall exponential decay. On resonance ($\Delta = 0$), this expression simplifies to

$$|a(t)| = e^{-\frac{\Sigma_{\kappa}}{4}t} \left| \cos(\Lambda_0 t) - \frac{\Delta_{\kappa}}{4\Lambda_0} \sin(\Lambda_0 t) \right|, \quad (25)$$

with $\Lambda_0 = \sqrt{g^2 - \left(\frac{\Delta_{\kappa}}{4}\right)^2}$. The intra cavity photon number, proportional to $|a(t)|^2$, is then given by

$$|a(t)|^2 = e^{-\frac{\Sigma_{\kappa}}{2}t} \left(1 + \left(\frac{\Delta_{\kappa}}{4\Lambda_0} \right)^2 \right) \cos^2(\Lambda_0 t + \phi), \quad (26)$$

with $\phi = \arctan\left(\frac{\Delta_{\kappa}}{4\Lambda_0}\right)$. This expression describes an exponentially decaying, Rabi-like exchange of energy between the cavity and plasmon modes, in agreement with the time-resolved response shown in the inset of Fig. 3(c).

ACKNOWLEDGMENTS

This work was supported by the RIKEN Hakubi Program, the RIKEN Center for Quantum Computing, JST-FOREST, the Hattori Hokokai Foundation, the National Natural Science Foundation of China (Grant No. 12474135), and the National Basic Research Program of China (Grant No. 2025YFA1411400). We are grateful to Prof. Jaw-Shen Tsai for granting us access to the Kelvinox 400HA dilution refrigerator. We thank Prof. Denis Konstantinov for useful discussions.

AUTHOR CONTRIBUTIONS

A.J. led the experiments and data analysis. Y.T. assisted with the experiments. I.G. and O.R. contributed to technical development and experimental implementation. I.J.B., T.G., H.I., A.J., and E.K. performed theoretical modeling and numerical simulations, with contributions from J.W. E.K. conceived and supervised the project. The manuscript was written by A.J., H.I. and E.K. with input from all authors.

Supplementary Information A: Approximated plasmon frequency calculation

To approximately obtain the plasmon frequency from Eq. 4, we extract an effective radius R^* and an effective uniform density n_0 from the simulated profile following Ref. 26. The wave number of the μ -th radial mode is determined by the boundary condition that the radial current vanishes at R^* , which is given by $J'_0(k_{0,\mu}R^*) = 0$, where J'_0 denotes the derivative of the zeroth-order Bessel function. We take R^* as the radius at which the simulated density drops to zero. With this R^* , the uniform electron density n_0 is obtained by approximating the density profile as a disk of radius R^* , whose total electron number matches that obtained from the simulated density profile in Fig. 2(b,d).

Fig. 2(d) shows the simulated electron density profiles corresponding to the resonances observed at $V_{\text{BC}} = 10, 9, 8$, and 7.5 V. For each value of V_{BC} , we select the resonance appearing at the most negative value of V_{BM} ($V_{\text{BM}}^{\text{sim}} = -14.2, -17.9, -23.1$, and -26.4 V, respectively). The corresponding pairs of $(k_{0,1}, n_0)$ for each density profile are listed in Table I. Substituting these values into Eq. 4 yields $\omega_p/2\pi \sim 125$ MHz in all cases, indicating that these resonances correspond to the fundamental radial plasmon mode. The deviation from $\omega_0/2\pi$ reflects the use of an effective uniform-density model. The thick red line in Fig. 2(b) corresponds to the density profile for $V_{\text{BC}} = 7.5$ V at $V_{\text{BM}}^{\text{exp}} = 0.8$ V. In this case, substituting $(k_{0,2}, n_0)$ (Table I) into Eq. 4 gives $\omega_p/2\pi = 130.5$ MHz, demonstrating that this resonance corresponds to the second radial plasmon mode.

TABLE I. Extracted parameters $(R^*, k_{0,\mu}, n_0)$ for representative resonances using the simulated density profiles (see, for example Fig. 2(b,d)) for the $V_{\text{BM}}^{\text{exp}}$ at which avoided level crossings in Fig. 2(a) and the corresponding μ -th plasmon frequencies ω_p calculated from Eq. 4. The corresponding simulated values $V_{\text{BM}}^{\text{sim}}$, at which avoided level crossings occur in the simulation (Fig. 2(c)), are also listed for comparison. OOR indicates the plasmon mode was outside the simulated V_{BM} range.

V_{BC} (V)	μ	$V_{\text{BM}}^{\text{exp}}$ (V)	$V_{\text{BM}}^{\text{sim}}$ (V)	R^* (cm)	$k_{0,\mu}$ (cm^{-1})	n_0 (10^7cm^{-2})	$\omega_p/2\pi$ (MHz)
10	1	-14.2	-13.8	0.3270	11.72	4.14	126.9
9	1	-17.9	-18.4	0.3150	12.16	3.81	125.0
8	1	-23.1	-24.0	0.2985	12.84	3.50	124.5
7.5	1	-26.4	-27.0	0.2910	13.17	3.41	125.0
10	2	4.0	OOR	0.3870	18.13	2.92	142.0
9	2	2.9	OOR	0.3780	18.56	2.65	137.3
8	2	1.5	3.8	0.3660	19.17	2.36	132.0
7.5	2	0.8	2.6	0.3600	19.49	2.26	130.5
6.0	2	-3.3	-2.2	0.3300	21.26	1.93	126.7
4.0	2	-14.3	-13.8	0.2745	25.56	1.51	123.9
6.0	3	1.9	4.6	0.3600	28.26	1.64	135.8
4.0	3	-3.5	-2.4	0.3090	32.92	1.20	125.9
6.0	4	3.5	OOR	0.3735	35.67	1.53	147.8
4.0	4	0.5	1.8	0.3330	40.01	1.03	128.5

Supplementary Information B: Reflection coefficient

The reflection coefficient of the LC resonator without plasmon (Eq. 1 with Eq. 2 in the limit $Z_p \rightarrow \infty$) can be approximated as

$$\Gamma_{\text{ref}} \approx 1 - \frac{2Q_{\text{tot}}/Q_{\text{ext}}}{1 + i 2Q_{\text{tot}} \left(\frac{\omega}{\omega_0} - 1 \right)} = 1 - \frac{-i \kappa_{\text{ext}}}{(\omega - \omega_0) - i \kappa/2} \quad (\text{B1})$$

for $C_c \ll C$. The resonator resonance frequency and the quality factors are given by

$$\omega_0 = \sqrt{\frac{1}{(C + C_c)L}}, \quad (\text{B2})$$

$$Q_{\text{int}}^{-1} = \frac{1}{R\omega_0 C} = \frac{\kappa_{\text{int}}}{\omega_0}, \quad (\text{B3})$$

$$Q_{\text{ext}}^{-1} = \frac{\omega_0 C_c^2 Z_0}{C} = \frac{\kappa_{\text{ext}}}{\omega_0}, \quad (\text{B4})$$

$$Q_{\text{tot}}^{-1} = \frac{1}{\omega_0 C} \left(\frac{1}{R} + \frac{(\omega_0 C_c Z_0)^2}{Z_0} \right) = \frac{\kappa}{\omega_0}. \quad (\text{B5})$$

The plasmon mode can be modeled as a linear harmonic oscillator characterized by a resonance frequency ω_p , a linewidth γ_p , and a coupling strength g to the resonator. As a result, its contribution to the circuit response appears as a frequency-dependent self-energy term, $\frac{g^2}{(\omega - \omega_p) + i \gamma_p/2}$, which, when incorporated into the resonator response, yields the reflection coefficient including the plasmon contribution (Eq. 3).

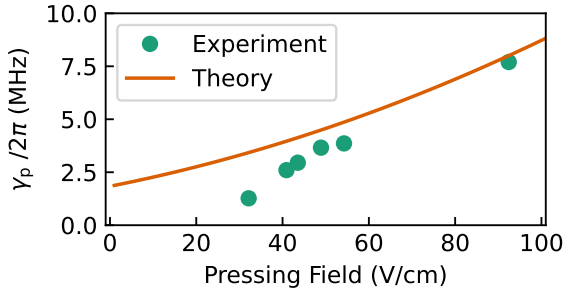


FIG. 5. Extracted values of $\gamma_p/2\pi$ as a function of pressing field measured at $T = 180$ mK. The pressing field corresponds to V_{BC}/D (for $V_{BC} = 10, 9, 8, 7.5, 6$ V) plus a correction for the field due to the image charge induced by the electrons, which is the electric field experienced by the electrons near the center. The value at $V_{BC} = 17$ V is extracted from Fig. 3(a), while the values at $V_{BC} = 10, 9, 8, 7.5, 6, 4$ V are extracted from Fig. 2(a). The value of γ_p for $V_{BC} = 4$ V in Fig. 2(a) could not be extracted from Fig. 2(a) as the plasmon frequency changes rapidly with the radius at higher modes. The orange line indicates $\gamma_p = 1/\tau$ from the model of Ref. 39 at $T = 180$ mK. The marker size is larger than the error.

Formula for the Split Resonance Peaks

We can rewrite Eq. 3 as $\Gamma_{\text{ref}} = \frac{A-iB}{A-iC}$, where

$$A = (\omega_0 - \omega) - \frac{g^2(\omega_p - \omega)}{(\omega_p - \omega)^2 + (\gamma_p/2)^2} \quad (\text{B6})$$

$$B = \frac{\kappa_{\text{int}} - \kappa_{\text{ext}}}{2} + \frac{g^2\gamma_p/2}{(\omega_p - \omega)^2 + (\gamma_p/2)^2} \quad (\text{B7})$$

$$C = \frac{\kappa_{\text{int}} + \kappa_{\text{ext}}}{2} + \frac{g^2\gamma_p/2}{(\omega_p - \omega)^2 + (\gamma_p/2)^2}. \quad (\text{B8})$$

When the denominator of Γ_{ref} vanishes, the system supports non-trivial solutions corresponding to the upper and lower hybridized eigenmodes, yielding the complex eigenfrequencies $\tilde{\omega}_{\pm}$ given in Eq. 20. At zero detuning, the amplitude of Γ_{ref} exhibits a pair of split resonance peaks when the mode-splitting parameter $\Lambda_0 = \sqrt{g^2 - \left(\frac{\Delta_{\kappa}}{4}\right)^2}$ is real. In this regime, the frequency separation between the two hybridized modes is $2\Lambda_0$.

We fitted the resonance peaks in Fig. 2(a), Fig. 3(a) and Fig. 4(a) using the expression

$$|\Gamma_{\text{ref}}| = \sqrt{\frac{A^2 + B^2}{A^2 + C^2}}, \quad (\text{B9})$$

from which we extracted the coupling strength g and the plasmon decay rate γ_p .

The pressing-field dependence of γ_p extracted from Fig. 2(a) and Fig. 3(a) is presented in Fig. 5. The extracted values for $V_{BC} = 10, 9, 8, 7.5, 6$ V from Fig. 2(a) are $\gamma_p/2\pi = 3.86 \pm 0.07, 3.66 \pm 0.04, 2.96 \pm 0.02, 2.60 \pm 0.04, 1.26 \pm 0.06$ MHz, and are used in the simulation

shown in Fig. 2(c). The value of γ_p at $V_{BC} = 4$ V in Fig. 2(a) could not be extracted because the plasmon frequency varies rapidly with radius for higher-order modes. Therefore, the value obtained at $V_{BC} = 6$ V was used in the simulations for $V_{BC} = 4$ V in Fig. 2(c).

The temperature dependence of γ_p , $\Delta = \omega_0 - \omega_p$, and g extracted from Fig. 4 (a) are shown in Fig. 4 (b-d). The values $\kappa_{\text{ext}}/2\pi = 0.20$ MHz and $\kappa_{\text{int}}/2\pi = 0.19$ MHz used in the fits were obtained from the plasmon-unperturbed (far-from-resonance) configuration [30].

Supplementary Information C: Coupling strength g

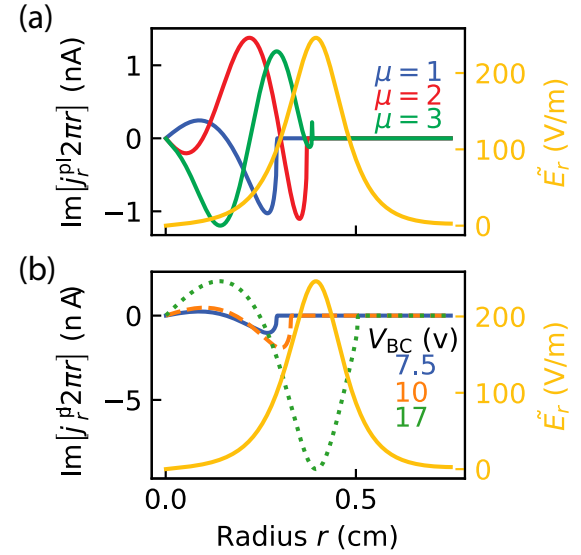


FIG. 6. Radial profiles of the product of the imaginary part of the plasmon current density and the circumference, $\text{Im}[j_r^p 2\pi]$, as a function of the radial coordinate r , together with the RF-induced electric field δE_r^{RF} , both calculated for a 1 V AC excitation applied to the top center electrode. The solid blue, red, green, and orange dashed lines are evaluated at the resonance conditions shown in Fig. 2(c), as detailed below: the blue solid lines in (a) and (b) correspond to the fundamental mode ($\mu = 1$) at $V_{BC} = 7.5$ V and $V_{BM} = -27$ V; the red line in (a) corresponds to the second mode ($\mu = 2$) at $V_{BC} = 7.5$ V and $V_{BM} = 2.6$ V, and the green line in (a) corresponds to the third mode ($\mu = 3$) at $V_{BC} = 6$ V and $V_{BM} = 4.6$ V; the orange dashed line in (b) corresponds to the fundamental mode ($\mu = 1$) at $V_{BC} = 10$ V and $V_{BM} = -13.8$ V. The green dotted line in (b) corresponds to the fundamental mode ($\mu = 1$) shown in Fig. 3(b), where $V_{BC} = V_{BM} = 17$ V and strong coupling is observed at $V_{BO} = -30.7$ V.

The coupling strength g between the LC resonator field and a plasmon eigenmode can be quantified by the reactive (imaginary) component of the power overlap between the plasmon-mode current density and the driving RF

electric field,

$$g \propto \text{Im} \left[\int \delta E_r^{\text{RF}}(r) j_r^{\text{pl}}(r) 2\pi r dr \right]. \quad (\text{C1})$$

Here, j_r^{pl} denotes the sheet current density of the plasmon mode, and δE_r^{RF} is the radial RF electric field generated by the RF excitation. Fig. 6 shows the radial profiles of $j_r^{\text{pl}}(r)$, $2\pi r$ and $\delta E_r^{\text{RF}}(r)$, both calculated for a unit AC excitation voltage. δE_r^{RF} reaches its maximum near $r \simeq 4$ mm, corresponding to the edge of the top center electrode. We numerically verified the validity of the linear relation in Eq. C1 by comparing the values of g extracted from the resonance splitting of the numerically simulated reflection spectra shown in Fig. 2(c) and Fig. 3(b) with the quantity $\text{Im} \left[\int \delta E_r^{\text{RF}}(r) j_r^{\text{pl}}(r) 2\pi r dr \right]$. A strong enhancement of the coupling strength g occurs when $j_r^{\text{pl}}(r)$, $2\pi r$ closely matches the spatial profile of $\delta E_r^{\text{RF}}(r)$, yielding a large overlap between the two fields, as demonstrated by the green dotted line in Fig. 6(b), where strong coupling is observed.

DERIVATION OF EQ. C1

We model the system as two coupled harmonic oscillators. The resonator mode is characterized by an amplitude $A_c(t)$ and an effective mass M_c , with kinetic and potential energies given by

$$K_c = \frac{1}{2} M_c \dot{A}_c^2, \quad U_c = \frac{1}{2} M_c \omega_0^2 A_c^2. \quad (\text{C2})$$

Similarly, the plasmon mode is described by an amplitude $A_p(t)$ and an effective mass M_p , with kinetic and potential energies

$$K_p = \frac{1}{2} M_p \dot{A}_p^2, \quad U_p = \frac{1}{2} M_p \omega_p^2 A_p^2. \quad (\text{C3})$$

Coupling between the resonator and plasmon modes is introduced through an interaction term

$$U_{\text{int}} = G A_c A_p, \quad (\text{C4})$$

where G quantifies the coupling strength. The corresponding Lagrangian is

$$L = \frac{1}{2} M_c \dot{A}_c^2 - \frac{1}{2} M_c \omega_0^2 A_c^2 + \frac{1}{2} M_p \dot{A}_p^2 - \frac{1}{2} M_p \omega_p^2 A_p^2 - G A_c A_p. \quad (\text{C5})$$

The Euler–Lagrange equations for $A_c(t)$ and $A_p(t)$ then read

$$M_c \ddot{A}_c + M_c \omega_0^2 A_c + G A_p = 0, \quad (\text{C6})$$

$$M_p \ddot{A}_p + M_p \omega_p^2 A_p + G A_c = 0. \quad (\text{C7})$$

Introducing a harmonic time dependence $A_{c,p}(t) \propto e^{-i\omega t}$, the equations of motion reduce to

$$(\omega_0^2 - \omega^2) A_c + G A_p / M_c = 0, \quad (\text{C8})$$

$$(\omega_p^2 - \omega^2) A_p + G A_c / M_p = 0. \quad (\text{C9})$$

Near resonance ($\omega \approx \omega_0$ and $\omega \approx \omega_p$), taking

$$a \equiv \sqrt{\omega_0 M_c} A_c, \quad b \equiv \sqrt{\omega_p M_p} A_p, \quad (\text{C10})$$

and

$$g \equiv \frac{G}{2\sqrt{\omega_0 \omega_p M_c M_p}}, \quad (\text{C11})$$

Eq. C8 and Eq. C9 are reduced to

$$(\omega_0 - \omega) a + g b = 0, \quad (\text{C12})$$

$$(\omega_p - \omega) b + g a = 0, \quad (\text{C13})$$

which is identical to Eq. 19 for $\gamma_p = \kappa = 0$.

The physical origin of the interaction can be understood in terms of electromagnetic work. In classical electrodynamics, the instantaneous power transferred from an electric field \mathbf{E} to a current density \mathbf{j} is given by $\dot{U} = \int \mathbf{E} \cdot \mathbf{j} dA$. For time-harmonic fields, only the reactive (non-dissipative) component contributes to coherent energy exchange between two lossless modes. Consequently, the coupling constant is determined by the imaginary part of the field–current overlap,

$$G A_c A_p = \frac{1}{\omega} \text{Im} \int \delta \mathbf{E}_{\text{RF}} \cdot \mathbf{j}_{\text{pl}} dA, \quad (\text{C14})$$

where the factor $1/\omega$ converts power into energy. Near resonance ($\omega_0 \approx \omega_p$), the coupling rate can finally be written as

$$g = \frac{\text{Im} \int \delta \mathbf{E}_{\text{RF}} \cdot \mathbf{j}_{\text{pl}} dA}{4\sqrt{U_c U_p}}. \quad (\text{C15})$$

Supplementary Information D: Effects of Wigner crystallization and RF Drive on the Plasmon Frequency and Decay

The RF excitation power differs between the measurements shown in Fig. 2 and Fig. 4 (-50 dBm) and Fig. 3 (-20 dBm), both specified at the output of the signal generator. The higher drive power is required in the time-domain experiment to excite the plasmon mode strongly enough for real-time observation.

To examine the influence of the RF drive on the resonance condition, we measured the same voltage configuration as in Fig. 3(a), but with a reduced RF power of -50 dBm (data not shown). Under these conditions, the resonance appears at $V_{\text{BO}} \approx -25$ V, instead of -29 V for the -20 dBm drive. As discussed in Sec. V, at the density $n_0 = 10^8 \text{ cm}^{-2}$ and at $T \approx 180 \text{ mK}$ the electron ensemble is expected to form a Wigner crystal. We attribute the shift of the resonance to more negative voltages observed at high RF power to approaching to the melting temperature due to heating. The simulated resonance position is found at $V_{\text{BO}} = -30.7$ V, slightly different from the low-power experimental value. This deviation

may be similarly due to the heating. Further discussion is provided in Ref. 50.

We also note that the measurements in Fig. 2 correspond to lower electron densities, where the system remains in the liquid phase.

Supplementary Information E: Temperature dependence of the LC resonator

Although the LC resonator has an overall temperature dependence due to the the temperature dependent characteristics of the various surface mount components comprising it, these changes are negligible compared with the temperature dependence of γ_p and Δ observed between 0.17 K and 0.9 K in Fig. 4. Fig. 7 shows fitting parameters of the bare LC resonator extracted from frequency sweeps at different temperatures. Over the temperature range from 0.17 K to 0.9 K, the resonance frequency changes by less than 0.07 MHz, and the total decay rate $\kappa/2\pi$ changes by only 0.02 MHz.

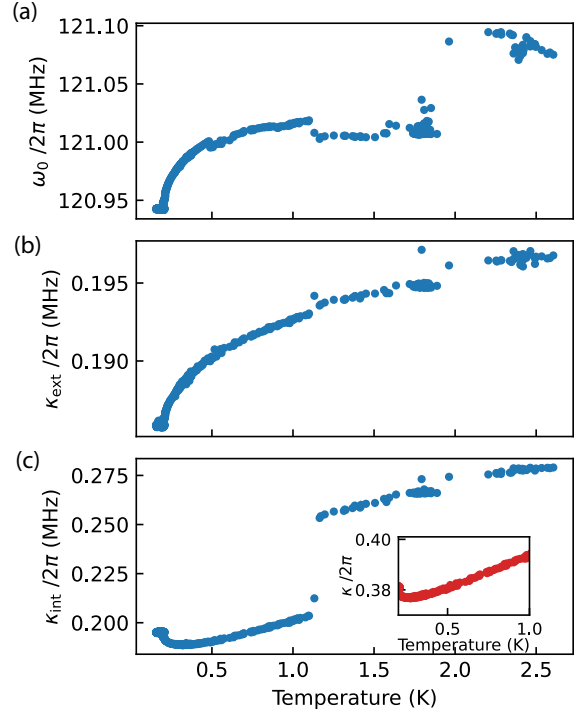


FIG. 7. The fitted bare LC resonator parameters as a function of the cell temperature for (a) the resonance frequency, (b) the external decay and (c) the internal decay. The large, sudden increase in κ_{int} is attributed to the superconducting transition of the aluminum bonding wires, which have a critical temperature of 1.175 K. (c) Inset: The total decay rate from 0.2 K to 1 K, the measurement range of Fig. 4.

[1] M. S. Tame, K. R. McEnergy, S. K. Özdemir, J. Lee, S. A. Maier, and M. S. Kim, Quantum plasmonics, *Nat. Phys.* **9**, 329 (2013).

[2] Y.-E. Liu, X. Shi, T. Yokoyama, S. Inoue, Y. Sunaba, T. Oshikiri, Q. Sun, M. Tamura, H. Ishihara, K. Sasaki, and H. Misawa, Quantum-coherence-enhanced hot-electron injection under modal strong coupling, *ACS Nano* **17**, 8315 (2023).

[3] N. Serpone and A. V. Emeline, Semiconductor photocatalysis - past, present, and future outlook, *J. Phys. Chem. Lett.* **3**, 673 (2012).

[4] C. Clavero, Plasmon-induced hot-electron generation at nanoparticle/metal-oxide interfaces for photovoltaic and photocatalytic devices, *Nat. Photonics* **8**, 95 (2014).

[5] M. W. Knight, H. Sobhani, P. Nordlander, and N. J. Halas, Photodetection with active optical antennas, *Science* **332**, 702 (2011).

[6] A. M. Shrivastav, U. Cvelbar, and I. Abdulhalim, A comprehensive review on plasmonic-based biosensors used in viral diagnostics, *Commun. Biol.* **4**, 70 (2021).

[7] S. L. Braunstein and P. van Loock, Quantum information with continuous variables, *Rev. Mod. Phys.* **77**, 513 (2005).

[8] S. Takada, G. Georgiou, J. Wang, Y. Okazaki, S. Nakamura, D. Pomaranski, A. Ludwig, A. D. Wieck, M. Yamamoto, C. Bäuerle, and N.-H. Kaneko, Eigenstate control of plasmon wavepackets with electron-channel blockade, *Nat. Commun.* **16**, 9942 (2025).

[9] K. Yoshioka, G. Bernard, T. Wakamura, M. Hashisaka, K.-I. Sasaki, S. Sasaki, K. Watanabe, T. Taniguchi, and N. Kumada, On-chip transfer of ultrashort graphene plasmon wave packets using terahertz electronics, *Nat. Electron.* **7**, 537 (2024).

[10] A. Gonzalez-Tudela, D. Martin-Cano, E. Moreno, L. Martin-Moreno, C. Tejedor, and F. J. Garcia-Vidal, Entanglement of two qubits mediated by one-dimensional plasmonic waveguides, *Phys. Rev. Lett.* **106**, 020501 (2011).

[11] N. S. Mueller, Y. Okamura, B. G. M. Vieira, S. Juergenssen, H. Lange, E. B. Barros, F. Schulz, and S. Reich, Deep strong light-matter coupling in plasmonic nanoparticle crystals, *Nature* **583**, 780 (2020).

[12] M. W. Cole and M. H. Cohen, Image-potential-induced surface bands in insulators, *Phys. Rev. Lett.* **23**, 1238 (1969).

[13] V. Shikin, Motion of helium ions near a vapor-liquid surface, Sov. Phys. JETP **31**, 936 (1970).

[14] Y. Monarkha and K. Kono, *Two-dimensional coulomb liquids and solids*, Springer Series in Solid-State Sciences (Springer, Berlin, Germany, 2004).

[15] E. Y. Andrei, *Two-Dimensional Electron Systems : on Helium and other Cryogenic Substrates* (Springer Netherlands, 1997).

[16] R. S. Crandall and R. Williams, Properties of electron surface states on liquid helium, Phys. Rev. A **5**, 2183 (1972).

[17] P. M. Platzman and M. I. Dykman, Quantum Computing with Electrons Floating on Liquid Helium, Science **284**, 1967 (1999).

[18] G. Koolstra, G. Yang, and D. I. Schuster, Coupling a single electron on superfluid helium to a superconducting resonator, Nat. Commun. **10**, 5323 (2019).

[19] X. Zhou, G. Koolstra, X. Zhang, G. Yang, X. Han, B. Dizdar, X. Li, R. Divan, W. Guo, K. W. Murch, D. I. Schuster, and D. Jin, Single electrons on solid neon as a solid-state qubit platform, Nature **605**, 46 (2022).

[20] X. Zhou, X. Li, Q. Chen, G. Koolstra, G. Yang, B. Dizdar, Y. Huang, C. S. Wang, X. Han, X. Zhang, D. I. Schuster, and D. Jin, Electron charge qubit with 0.1 millisecond coherence time, Nat. Phys. **20**, 116 (2024).

[21] A. Jennings, X. Zhou, I. Grytsenko, and E. Kawakami, Quantum computing using floating electrons on cryogenic substrates: Potential and challenges, Appl. Phys. Lett. **124**, 120501 (2024).

[22] G. Koolstra, E. O. Glen, N. R. Beysengulov, H. Byeon, K. E. Castoria, M. Sammon, S. A. Lyon, D. G. Rees, and J. Pollanen, Strong coupling of a microwave photon to an electron on helium, (2025), arXiv:2509.14506.

[23] C. C. Grimes and G. Adams, Plasmons in a sheet of electrons on liquid helium, Surf. Sci. **58**, 292 (1976).

[24] C. C. Grimes and G. Adams, Observation of two-dimensional plasmons and electron-riplon scattering in a sheet of electrons on liquid helium, Phys. Rev. Lett. **36**, 145 (1976).

[25] E. Andrei, 2d electron systems viewed through an rf spectrometer, Physica B **197**, 335 (1994).

[26] D. C. Glattli, E. Y. Andrei, G. Deville, J. Poitrenaud, and F. I. Williams, Dynamical hall effect in a two-dimensional classical plasma, Phys. Rev. Lett. **54**, 1710 (1985).

[27] O. I. Kirichek, K. Shirahama, and K. Kono, Plasma resonance of the wigner solid on the free surface of normal and superfluid 3he, J. Low Temp. Phys. **113**, 1103 (1998).

[28] C. A. Mikolas, N. R. Beysengulov, A. J. Schleusner, D. G. Rees, C. Undershute, and J. Pollanen, Plasmon mode engineering with electrons on helium, Nat. Commun. **16**, 4959 (2025).

[29] Y. Iye, Mobility of electrons in the surface state of liquid helium, J. Low Temp. Phys. **40**, 441 (1980).

[30] A. Jennings, I. Grytsenko, Y. Tian, O. Rybalko, J. Wang, I. J. Barabash, and E. Kawakami, Probing the quantum capacitance of rydberg transitions of surface electrons on liquid helium via microwave frequency modulation, Phys. Rev. Lett. **135**, 087001 (2025).

[31] R. Williams, R. S. Crandall, and A. H. Willis, Surface states of electrons on liquid helium, Phys. Rev. Lett. **26**, 7 (1971).

[32] Although phasor analysis typically assumes a time dependence of $e^{i\omega t}$, here we follow the convention used in Eq. 9 and adopt $e^{-i\omega t}$ as the time dependence. This choice is made to ensure consistency with the input-output theory employed in the analysis. As a consequence, the imaginary unit i appears with an overall sign change throughout the expressions.

[33] M. L. Ott-Rowland, V. Kotsubo, J. Theobald, and G. A. Williams, Two-dimensional plasma resonances in positive ions under the surface of liquid helium, Phys. Rev. Lett. **49**, 1708 (1982).

[34] L. Wilen and R. Giannetta, Impedance methods for surface state electrons, J. Low Temp. Phys. **72**, 353 (1988).

[35] T. Giovansili, I. J. Barabash, A. Jennings, and E. Kawakami, Electron density simulation code, https://github.com/erikawa-e/density_profile (2025), GitHub repository.

[36] Q. Zhang, M. Lou, X. Li, J. L. Reno, W. Pan, J. D. Watson, M. J. Manfra, and J. Kono, Collective non-perturbative coupling of 2d electrons with high-quality-factor terahertz cavity photons, Nat. Phys. **12**, 1005 (2016).

[37] X. Zhang, C.-L. Zou, L. Jiang, and H. X. Tang, Strongly coupled magnons and cavity microwave photons, Phys. Rev. Lett. **113**, 156401 (2014).

[38] E. Kawakami, A. Elarabi, and D. Konstantinov, Relaxation of the excited rydberg states of surface electrons on liquid helium, Phys. Rev. Lett. **126**, 106802 (2021).

[39] M. Saitoh and T. Aoki, Theory of Hot Electrons on the Liquid ${}^4\text{He}$ Surface, J. Phys. Soc. Jpn. **44**, 71 (1978).

[40] H. Isshiki, D. Konstantinov, H. Akimoto, K. Shirahama, and K. Kono, Microwave Absorption of Surface-State Electrons on Liquid ${}^3\text{He}$, J. Phys. Soc. Jpn. **76**, 094704 (2007).

[41] R. Mehrotra, C. J. Guo, Y. Z. Ruan, D. B. Mast, and A. J. Dahm, Density-dependent mobility of a two-dimensional electron fluid, Phys. Rev. B Condens. Matter **29**, 5239 (1984).

[42] H. Ikegami, K. Kim, D. Sato, K. Kono, H. Choi, and Y. P. Monarkha, Anomalous quasiparticle reflection from the surface of a ${}^3\text{He}$ - ${}^4\text{He}$ dilute solution, Phys. Rev. Lett. **119**, 195302 (2017).

[43] C. C. Grimes and G. Adams, Evidence for a liquid-to-crystal phase transition in a classical, two-dimensional sheet of electrons, Phys. Rev. Lett. **42**, 795 (1979).

[44] R. H. Morf, Temperature dependence of the shear modulus and melting of the two-dimensional electron solid, Phys. Rev. Lett. **43**, 931 (1979).

[45] H. Ikegami, H. Akimoto, and K. Kono, Melting of a quasi-one-dimensional wigner crystal: Electrons on superfluid ${}^4\text{He}$ in a narrow channel, Phys. Rev. B Condens. Matter Mater. Phys. **82**, 201104 (2010).

[46] Y. P. Monarkha and V. E. Sivokon, A two-dimensional wigner crystal (review article), Low Temp. Phys. **38**, 1067 (2012).

[47] Y. P. Monarkha and K. Kono, High-frequency conductivity and phonon damping of a two-dimensional wigner solid on a free surface of liquid 3he, J. Phys. Soc. Jpn. **70**, 1617 (2001).

[48] S. A. Prasad and G. J. Morales, Equilibrium and wave properties of two-dimensional ion plasmas, Phys. Fluids **30**, 3475 (1987).

[49] T. Giovansili, I. J. Barabash, A. Jennings, and E. Kawakami, Plasmon simulation code, <https://github.com/erikawa-e/plasmon> (2025), GitHub repository.

[50] A. Jennings *et al.* (2026), in preparation.